



ELSEVIER

Contents lists available at ScienceDirect

## Deep-Sea Research II

journal homepage: [www.elsevier.com/locate/dsr2](http://www.elsevier.com/locate/dsr2)

# A numerical study of coupled estuary–shelf circulation around the Pearl River Estuary during summer: Responses to variable winds, tides and river discharge

Tingting Zu<sup>a,b</sup>, Jianping Gan<sup>a,\*</sup>

<sup>a</sup> Department of Mathematics & Division of Environment, The Hong Kong University of Science and Technology, Kowloon, Hong Kong, China

<sup>b</sup> State Key Laboratory of Tropical Oceanography, South China Sea Institute of Oceanography, Chinese Academy of Sciences, Guangzhou 510301, China

## ABSTRACT

The mean (sub-tidal) circulations in the Pearl River Estuary (PRE) and over the adjacent shelf are interactive. They are driven by multi-forcing of winds, tides, and the buoyancy of river discharge. Utilizing a validated three-dimensional, high resolution numerical model, we find that the circulation in the PRE during summer is dominated by an advective gravitational two-layer circulation in the upper estuary and the landward part of the lower PRE, where the surface flow pattern also varies with the upwelling winds. The circulation in the seaward part of the lower PRE is governed by both gravitational circulation and geostrophic intrusive current from the shelf. The pattern and intensity of these circulations are largely modulated by variable wind forcing. The cross-shore upwelling shelf circulation off the PRE enhances the water exchange rate between the shelf and the PRE, but the net intrusive transport into the PRE is negatively correlated with the intensity of upwelling-favorable wind stress. Relatively strong water exchange rate between the shelf and estuary occurs during upwelling, which reduces the flushing time of the estuary. Although the ebbing/flooding tide strengthens/weakens the eastward alongshore upwelling current, tidal effect on the upwelling circulation and on the net transport between the shelf and estuary is not significant over the sub-tidal period. The shelf influences the estuary mainly through the intrusions of the shelf waters at the western bank and along the two navigation channels of the PRE; and they are governed by geostrophic cross-shelf upwelling circulation and by gravitational intrusive currents due to pressure gradients, yielded by the alongshore variation of the upwelling shelf circulation and by the buoyancy forcing of the river plume, respectively.

© 2013 Elsevier Ltd. All rights reserved.

## 1. Introduction

The Pearl River Estuary (PRE) is located along the coast of Guangdong province in China between 21°N and 23°N, 113°E and 115°E (Fig. 1). It links the Pearl River, the world's 13th largest river with annual mean discharge rate:  $\sim 10,000 \text{ m}^3 \text{ s}^{-1}$ , with the continental shelf in the Northern South China Sea (NSCS). The river has 8 inlets, and 4 of them constitute more than half of the total discharge. These 4 inlets are located within the PRE along its western shore. The bell-shaped PRE has an axial length of  $\sim 60 \text{ km}$  with a narrow head of only several kilometers in the upper estuary near Hu Men (HM). It has a relatively wide seaside entrance of  $\sim 50 \text{ km}$  in the lower estuary between Hong Kong (HK) and Macau (MC) (Fig. 1). The estuary is characterized by a wide flat western bank less than 5 m deep, and by a relatively deep eastern valley. Two distinct deep channels of  $\sim 20 \text{ m}$  in

the central and eastern parts link the lower and upper PRE with the adjacent shelf. Over the shelf, the isobaths are approximately parallel to the coast with a strong cross-shelf gradient on the shelf to the west of the PRE. In contrast, the shelf slope farther offshore is steeper to the east of the PRE. In addition, the coastline is extremely complex around the PRE and adjacent shelf with many islands scattered around the entrance and many coastal bays. All these geometric and topographic features greatly modulate the circulation in both the estuary and the adjacent shelf.

Tides are mainly semi-diurnal (M2) and diurnal (K1) around the PRE region and have  $\sim 1.0 \text{ m}$  magnitude inside the PRE. They are amplified and modulated as they propagate back and forth in the PRE with spatially variable water depth. Tides form a counter-clockwise tidal residual circulation (Mao et al., 2004) and may affect the estuarine circulation in both tidal and sub-tidal frequencies. With the seaward freshwater from Pearl River discharge, they lead to a gravitational circulation in the PRE and exhibits as a salt wedge estuary in the wet season (Lu and Gan, this issue).

\* Corresponding author.

E-mail address: [magan@ust.hk](mailto:magan@ust.hk) (J. Gan).

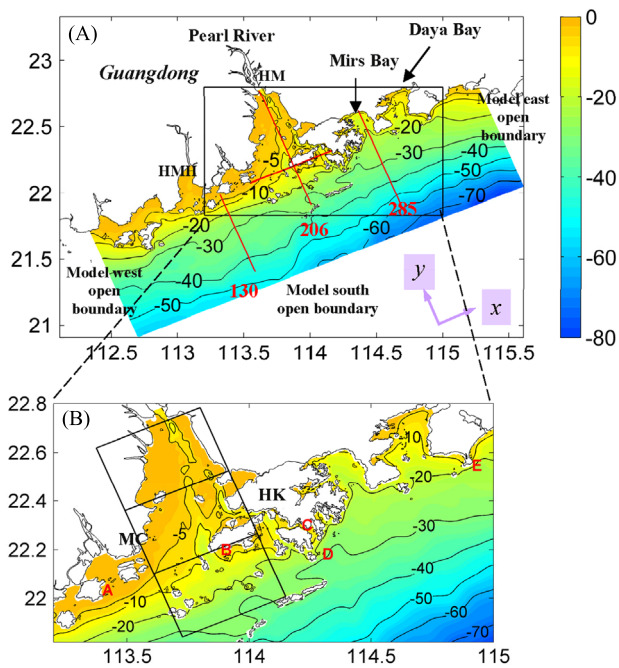


**Fig. 1.** (A) The model domain and bathymetry (m, color contour with black contour lines). The red lines denote the sections along the axial of the PRE (central), western and eastern shelves, as well as along the entrance of the PRE; (B) zoomed topography around the PRE and Hong Kong waters. The black boxes define the regions of upper, lower estuary and the shelf in the discussion. "A, B, C, D, E" represent the location of the tidal gauge in Sanzao, Shekpiik, HK-B, Waglan, and Gangkou respectively. (For interpretation of the references to color in this figure legend, the reader is referred to the web version of this article.)

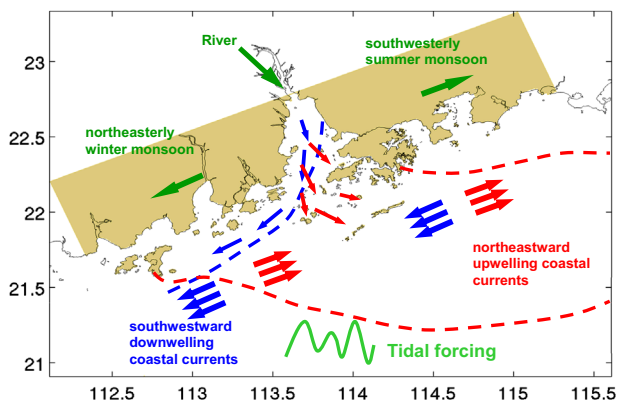


**Fig. 2.** Sketch of the river plume and coastal currents in the PRE and adjacent shelf in winter (blue dashed lines and arrows) and summer (red dashed lines and arrows), drawn based on the results from previous studies. Monsoon wind directions are also marked in the land points and the dashed lines refer to the outer edge location of the river plume. (For interpretation of the references to color in this figure legend, the reader is referred to the web version of this article.)

Besides the tidal forcing and buoyancy from river discharge, the circulation in the PRE is also forced by the winds and it interacts with the shelf circulation. The seasonal circulation and associated forcing in the PRE and adjacent shelf can be summarized based on the previous studies (e.g. Xue et al., 2001; Wong et al., 2003a,b; Su, 2004; Dong et al., 2004; Ou et al., 2007; Gan et al., 2009a,b; Sheng et al., 2010; Ji et al., 2011a,b), as shown in Fig. 2. Driven by the East Asia summer monsoon, coastal upwelling with the northeastward along-shore currents forms along the coast off the PRE. This wind-driven coastal current closely interacts with the estuarine circulation in the lower part of the PRE (Dong et al., 2004). Shelf water intrusion into the estuary occurs during the upwelling season (Zu and Gan, 2009). The intrusion may alter

circulation in the PRE and the water exchange rate between shelf and estuary. Although the tidal circulation plays an important role in the water exchange over the tidal cycle, sub-tidal circulation ultimately determines the net water exchange. The specific characteristics of these processes and the dynamics of the intrusion over the sub-tidal period remain largely unknown.

In addition, the fresher water exiting from the estuary forms a buoyant plume over the shelf. It spreads eastward or southeastward in response to the southwesterly monsoon during summer. The interaction of plume and wind-driven shelf circulation alters the intensity and pattern of the coastal upwelling circulation (Gan et al., 2009b) that, in turn, modulates the intrusion of shelf water into the PRE.

This study presents the processes and dynamical rationalization for variable responses of coupled estuary–shelf circulation in the PRE to the multi-forcing of wind, tide, river discharge and shelf circulation.

## 2. Ocean model

In this study, we use the free-surface, stretched terrain-following, hydrostatic, primitive-equation Regional Ocean Modeling System (ROMS) (Haidvogel et al., 2000; Shchepetkin and McWilliams, 2005). The model domain covers both the PRE and the adjacent shelf in order to link the two systems (Fig. 1A). The western and eastern boundaries are approximately normal to the isobaths over the shelf and extend about 150 km offshore from the coast. The southern open boundary is roughly along the 50 m isobath, about 100 km offshore from the PRE. We obtain the bottom topography by combining water depth data from the Hong Kong Maritime Department and water depths digitized from the high resolution navigation charts published by the China Maritime Safety Administration. The topography is slightly smoothed to reduce truncation error and the minimum water depth was set equal to 2 m. We adopt a horizontal curvilinear grid with  $400 \times 200$  grid points on the  $x$ -axis (alongshore) and  $y$ -axis (cross-shore). The grid forms an average horizontal grid size of about 0.8 km. We use the terrain-following  $s$ -ordinate (Song and Haidvogel, 1994) with 30 levels in the vertical axis and with higher resolution in both the surface and bottom boundary layers.

We initialize the model with horizontally uniform temperature and salinity profiles obtained from the World Ocean Atlas 2001 (WOA01; Boyer et al., 2005) at  $114.5^\circ\text{E}$ ,  $21.5^\circ\text{N}$ , which resembles the conditions found during a field cruise that carried out in July 2000. The initial sea surface elevation and current velocity are set to zero. We apply a temporally variable wind stress that was measured from July 1 to August 1, 2000 on Waglan Island (marked by D in Fig. 1B). Owing to the relatively weak spatial variation of wind forcing in the PRE region, the wind stress is applied uniformly throughout the whole model domain. The time series of wind contains two  $\sim 10$ -day typical upwelling periods separated by one  $\sim 8$ -day upwelling relaxation or weak downwelling period (Fig. 3). The time series represents the typical variation in the southwesterly monsoon wind in the region. The wind stress is calculated using Large and Pond (1981), and is low-pass filtered using a 12-h filter to reduce spurious noise in the numerical solution.

We use tidal harmonic constituents of 8 major components ( $M_2$ ,  $K_1$ ,  $S_2$ ,  $O_1$ ,  $N_2$ ,  $P_1$ ,  $K_2$ , and  $Q_1$ ) extracted from the South China Sea tidal assimilation model (Zu et al., 2008) to provide the tidal elevation and currents on the model's open boundaries. We apply an observed time-dependent river discharge rate at the eight main river exits during the simulation period (Fig. 3B). The volume of discharge is uniformly distributed in the water column with river water temperature and salinity set to be  $29.5^\circ\text{C}$  and 3 psu. The

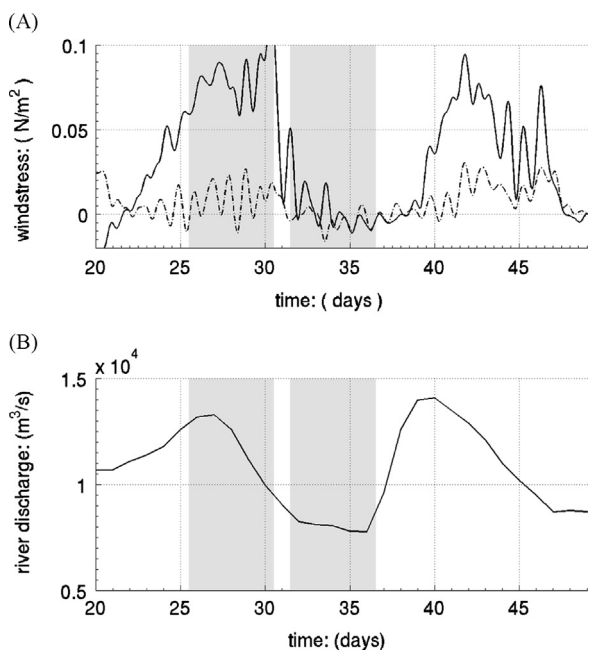


**Fig. 3.** (A) Time series of the 12 h smoothed wind stresses observed in Waglan Island (station D in Fig. 1B), the solid and dash-dot lines denote the wind stress in alongshore ( $y$ , positive directing northeast) and cross-shore ( $x$ , positive directing northwest) directions, respectively; (B) time series of daily averaged Pearl River discharge rate during July, 1st–August, 19th, 2000. The  $x$ -axis of the figure is the number of days from 1st, July. The gray windows in (A) and (B) denote the upwelling and upwelling relaxation periods, during which the simulation results are averaged.

buoyant forcing caused by heat and salt fluxes between the atmosphere and the sea surface are neglected in all cases for simplicity.

Along the open boundaries, we define the sea surface elevation,  $\zeta$ , using the implicit gravity-wave radiation boundary condition (Chapman, 1985). We apply Flather's open boundary condition (Flather, 1976) to the depth-averaged barotropic velocity in which the external information is provided by tidal elevation and currents (from both tide and wind-driven components). At the model's western and eastern boundaries, we use the Orlanski-type radiation open boundary condition (Orlanski, 1976), for the baroclinic velocity, temperature, and salinity. The phase speed is calculated using the unforced component of the baroclinic current according to Gan and Allen (2005). In this study, the external sub-tidal flows in the alongshore direction are provided by the results obtained from the cross-shelf two-dimensional model along the eastern and western open boundaries, similar to Gan and Allen (2005). At the southern boundary, the passive radiation condition is used for velocity, temperature, and salinity.

We use the Mellor and Yamada (1982) level 2.5 turbulent closure scheme to parameterize the vertical mixing. The viscosity/diffusivity coefficient,  $10 \text{ m}^4 \text{ s}^{-1}$  is used for the bi-harmonic horizontal mixing in momentum and tracer equations. The analysis is based on the hourly- or daily-averaged model output of the last 30 days from July 1 to August 19, 2000.

### 3. Model-observation comparison

We first show the observed sea surface elevation anomalies from tidal gauge measurements for stations at Sanzao, Shekpi, HK-B, Waglan, and Gangkou (stations A, B, C, D, and E in Fig. 1B) and compare them with simulated results in tidal (hourly data) and sub-tidal ( $\sim 36$  h, low-pass filtered data) frequency bands (Fig. 4).

The hourly observed elevation anomaly show that both semi-diurnal and diurnal tidal signals are important in this region. The elevation amplitude is  $\sim 1$  m for higher high and lower low water during spring tide and  $\sim 0.5$  m during neap tide. However, the amplitude of the sub-tidal elevation anomaly is less than 0.1 m during upwelling and upwelling relaxation periods. Although it is much smaller than the amplitude induced by the tides, the variation of the sub-tidal elevation reflect the pressure field for the residual current and transport. The temporal elevation anomalies with and without tides have a good correlation with the along-shore wind stress: the two periods of negative anomaly are associated with the upwelling favorable winds, and the positive anomaly is attributed to upwelling relaxation (i.e. weak downwelling). There are also small undulations embedded within main variations. Since the circulation in the estuary and adjacent shelf is mainly forced by time-dependent tide, wind and buoyancy from river discharge, the overall reasonably good agreements between observed and simulated time series of the elevation around the estuary over both intra- and sub-tidal temporal scales, indicate that the circulation variability is reasonably well captured by the model.

Since the biological phytoplankton bloom occurs in the nutrient-rich river water, we use the available surface chlorophyll- $a$  concentrations obtained from satellite remote sensing to qualitatively compare with the simulated surface salinity during the simulated period (Fig. 5). Similar spatial characteristics between them during upwelling (August 10) and upwelling-relaxation (August 19) suggest that the river plume and thus the flow field, which are controlled by river discharge, estuarine and wind-driven shelf circulation, are reasonably well simulated. Both model and observation show that the river plume extend farther offshore during upwelling wind due to strong surface Ekman current and river discharge; it has a shorter offshore but longer alongshore excursion during upwelling relaxation wind when river discharge and southwesterly wind are weakened.

## 4. Coupled estuarine-shelf circulation

### 4.1. Circulation during upwelling and upwelling relaxation winds

After filtering the tidal signals, the model outputs are averaged during upwelling period (from day 25.5 to day 30.5) and upwelling relaxation period (from day 31.5 to day 36.5), shown by the gray windows in Fig. 3. Fig. 6A shows that during the upwelling period, the depth-averaged currents are mainly seaward with a magnitude of  $\sim 0.05 \text{ m s}^{-1}$  in the upper estuary and in the central and eastern parts of the lower estuary, but are landward over the shallower western bank of the lower estuary, because of the intrusion of upwelling currents from the shelf. Over the shelf, the upwelling alongshore current directs mainly eastward but deviates alternatively northward/southward following the local topography. The shelf current speed is  $\sim 0.1 \text{ m s}^{-1}$  directly south of the PRE. The strongest alongshore currents are located over the eastern shelf, southeast of HK, where the velocity magnitude reaches  $0.4\text{--}0.5 \text{ m s}^{-1}$ . The asymmetry of the alongshore coastal upwelling jet is associated with the magnitude of the negative cross-shelf pressure gradient force (PGF) induced by steepness of the shelf, as shown in the corresponding sea surface elevation anomaly in Fig. 7A. This eastern intensification is absent in the model experiment with symmetric shelf topography (Zu and Gan, 2009).

The surface currents flow eastward in the entire PRE during the upwelling period (Fig. 6C). The bottom currents deviate substantially from the surface flow, directing mainly seaward in the upper PRE and landward in the lower PRE (Fig. 6E). Over the shelf, the surface currents are generally similar to the depth-averaged

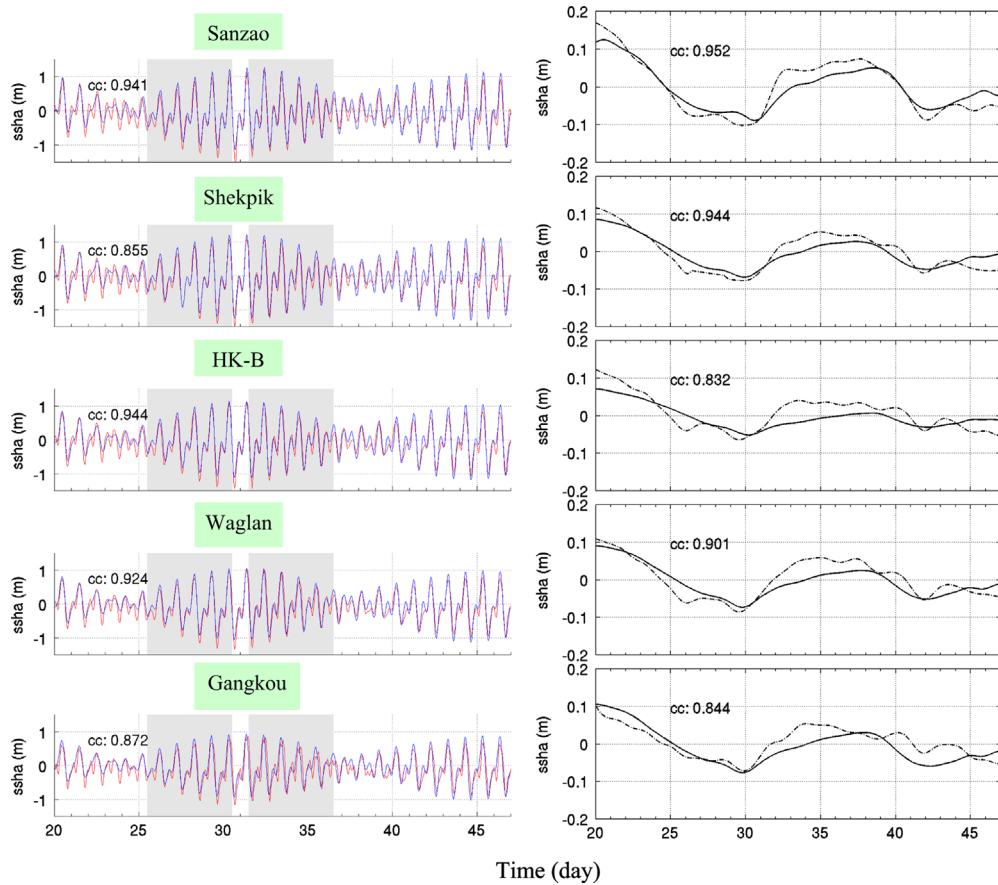


**Fig. 4.** Comparison of the hourly (left column) and inertial period ( $\sim 36$  h) smoothed (right column) sea surface elevation anomaly between simulated results and tidal gauge observation data in Sanzao, Shekpik, HK-B, Waglan, and Gangkou, respectively. The simulated and observed results are shown by the blue and red lines in the left column and by solid and dash-dot lines in the right column, respectively. The number shown in each figure is the correlation coefficient. The x-axis is the number of days from 1st, July, 2000. (For interpretation of the references to color in this figure legend, the reader is referred to the web version of this article.)

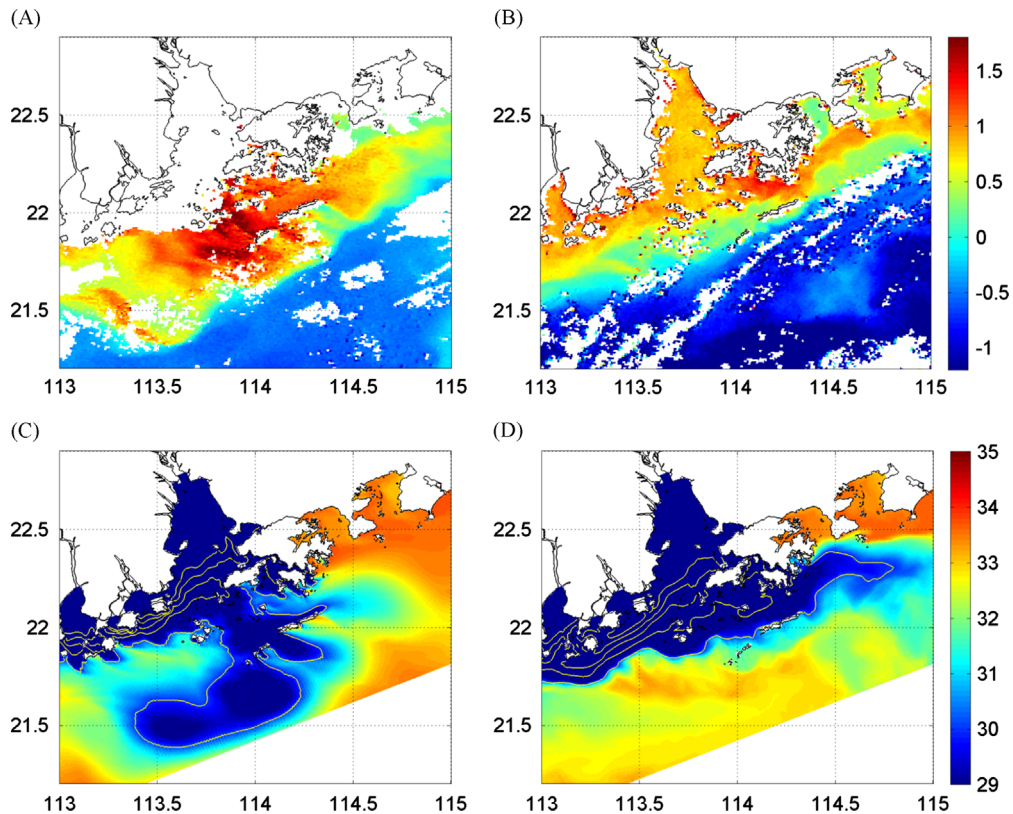


**Fig. 5.** Logarithm of the SeaWiFS Chl-a concentration ( $\log(\text{mg}/\text{m}^3)$ ) during (A) upwelling (10th, August, 2000) and (B) upwelling relaxation (19th, August, 2000). Their corresponding simulated salinity fields are shown by (C) and (D), respectively.

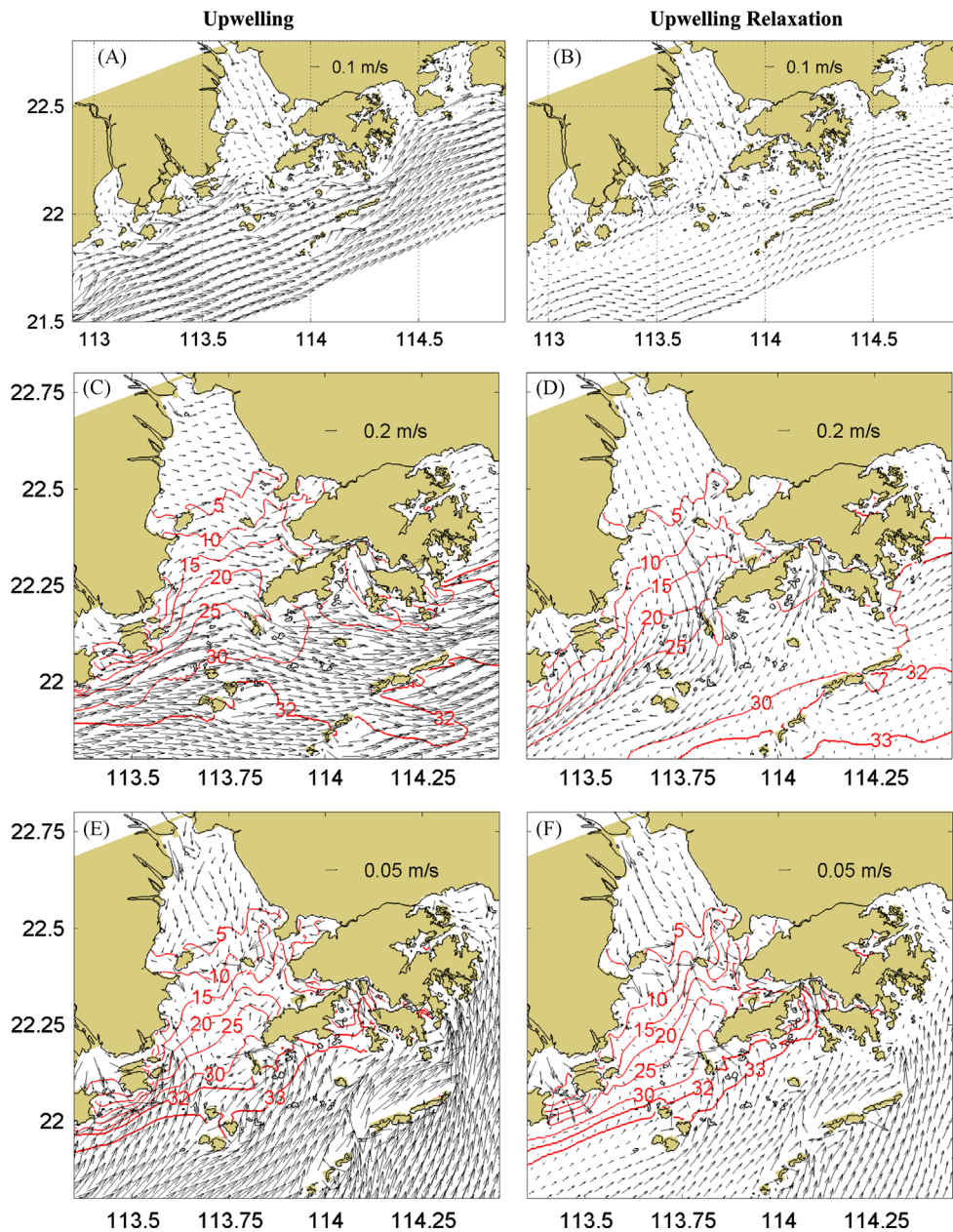


**Fig. 6.** Depth-averaged (A and B), surface (C and D), and bottom (E and F) residual velocity vectors and salinity distribution (red contour lines) averaged during upwelling (left column) and upwelling relaxation (right column). (A) and (B) are plotted to include the shelf region and (C–F) are plotted for the PRE region. (For interpretation of the references to color in this figure legend, the reader is referred to the web version of this article.)

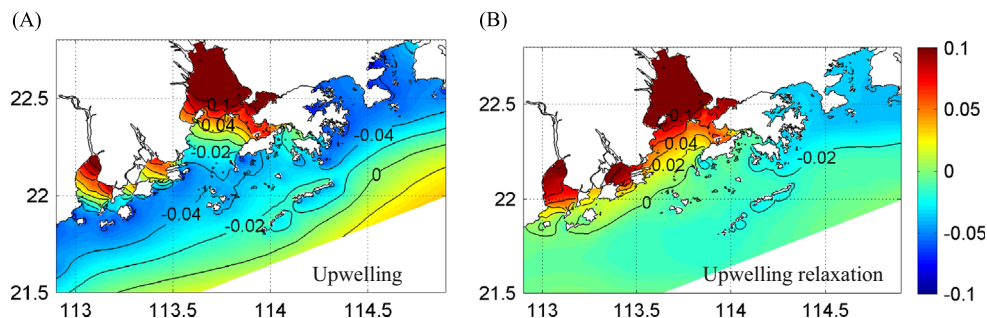


**Fig. 7.** Sea surface elevation anomaly (m) averaged during (A) upwelling and (B) upwelling relaxation.

current (Fig. 6C), while the bottom currents direct more landward. The upwelling current intrudes into the PRE from its western bank over the entire water column but with relatively strong magnitude

in the bottom. The bottom intrusion also occurs in the middle and eastern parts of the lower estuary. The surface freshwater exits the estuary from the middle and eastern parts of the entrance (Fig. 6C

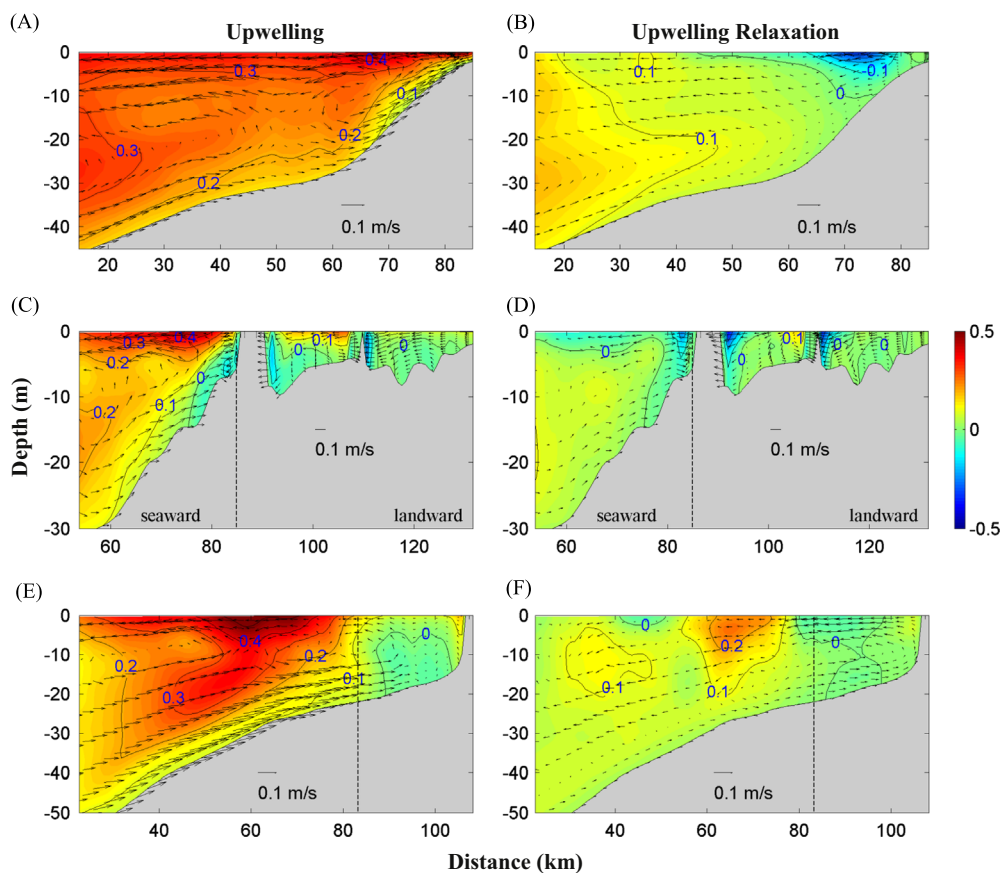


**Fig. 8.** Alongshore residual currents ( $\text{m s}^{-1}$ , contour lines and color contours) and cross-shelf circulation averaged during upwelling (left column) and upwelling relaxation (right column) along the sections shown in Fig. 1A. (A) and (B) are along the western shelf at slice  $x=130$ , (C) and (D) are along the axial of the PRE at slice  $x=206$ , (E) and (F) are along the eastern shelf at slice  $x=285$ . The  $x$  axis is the distance (km) from the southern boundary to the northern boundary of the model domain, and the  $y$  axis is the water depths (m). The vertical velocity component is multiplied by  $5 \times 10^2$  before plotting. The dash lines in (C–F) denote the locations of the entrance of the PRE (slice  $x=206$ ) and Mirs Bay (slice  $x=285$ ), respectively. (For interpretation of the references to color in this figure legend, the reader is referred to the web version of this article.)

and E). The saline seawater carried by the deep intrusive current reaches mid-estuary and forms a salinity front and a strong elevation gradient (Fig. 7) between the upper and lower estuary (Fig. 6). Both geostrophic and the gravitational currents play important roles in these intrusions, as will be discussed in Section 5. It is interesting to note that in spite of the difference in the flow fields, the horizontal salinity structures of the surface and bottom are quite similar inside the PRE. Evidently, strong vertical mixing occurs in the PRE; the mixing is mainly induced by tides, which weaken the intrusive flow.

As the upwelling favorable wind relaxes, the coastal currents weaken dramatically (Fig. 6B, D and F), but a weak eastward upwelling flow remains at depths over the shelf. The surface intrusive currents near the entrance during upwelling are replaced by strong southwestward currents (Fig. 6D). The shift of the current regime in the lower estuary is also evidently reflected in the sea surface elevation anomaly, in which the isolines of elevation rotate from the northwest–southeastward during upwelling to the northeast–southwestward during upwelling relaxation (Fig. 7B). Contrary to the conditions at the surface, the landward intrusion remains in the bottom layer, although its magnitude is substantially reduced. In the eastern part of the lower estuary, the lighter surface water advects southwestward towards the shelf while the shoreward intrusion of seawater strengthens slightly beneath it and pushes seawater farther northward during the upwelling relaxation (Fig. 6F).

It is clear that strong wind forcing during upwelling period not only affects the orientation of the flow field in the upper estuary, but also leads to the intrusion of shelf water from the western

bank in the lower estuary. When the upwelling favorable wind relaxes, the intrusion in the western bank weakens. The landward intrusion also occurs in the bottom layer along the middle and eastern channels in the lower estuary during upwelling, and this intrusion strengthens slightly during upwelling relaxation.

The responses of three-dimensional currents over the shelf and in the estuary to upwelling and upwelling–relaxation winds are shown by velocities, salinity, and vertical viscosity along the cross-sections (locations shown in Fig. 1A) on the western, middle, and eastern sides of the PRE (Figs. 8 and 9). During upwelling, the alongshore current has a jet-like structure over the shelf, which deepens and strengthens in the eastern shelf, but is relatively weak in the central shelf south of the PRE. There is a relatively strong vertical shear in the jet in the highly stratified water column in the central and eastern sections, where the cross-shelf circulation strengthens beneath the jet core, through the intrusion in the bottom frictional layer and extrusion in the surface frictional layer in particular.

The saline water advances shoreward in the bottom boundary layer along the three sections (Figs. 8A, C, E and 9A, C, E), which is weakened in the regions with relatively strong vertical mixing as shown by salinity and kinematic viscosity. The strengthened vertical mixing at mid-shelf along the western section is induced by the island effect upstream, where the alongshore current bifurcates around the island and forms strong spatial variability in the flow field (Figs. 8A and 9A). Relatively strong mixing also occurs at the entrance of the Mirs Bay (Fig. 9E) at the lee of Hong Kong Island and in the bay. Strong mixing also exists in the upper PRE due to tidal amplification.

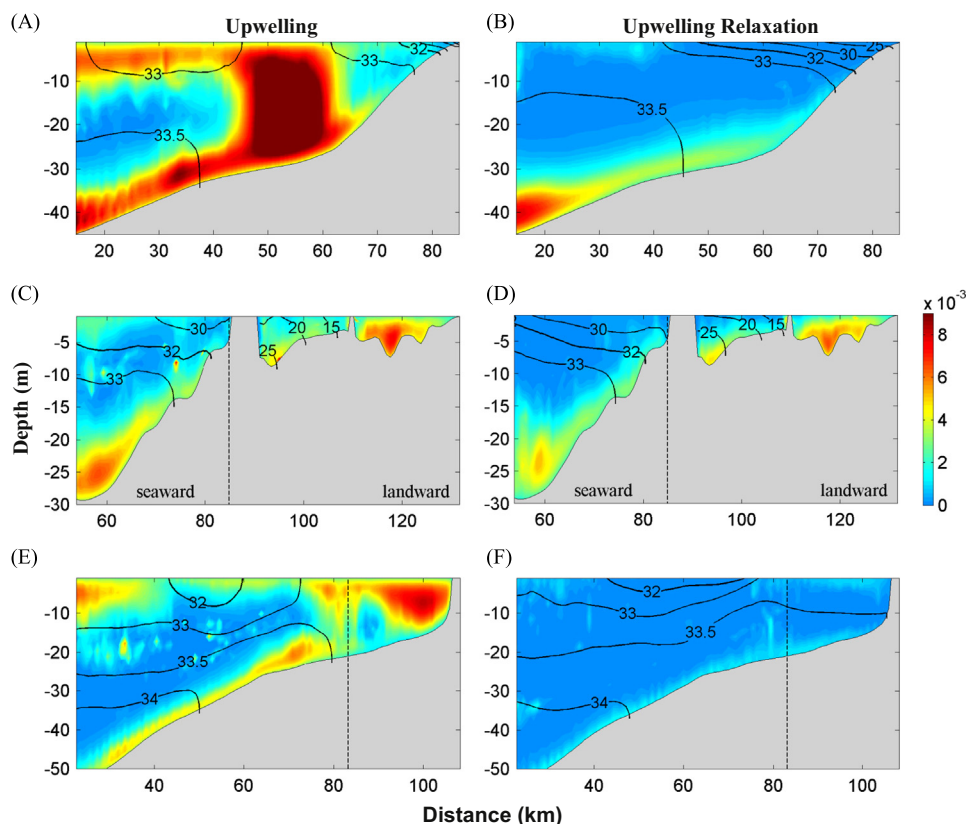


**Fig. 9.** Same as Fig. 8, but for salinity (black contour lines) and kinematic viscosity ( $\text{m}^2 \text{s}^{-1}$ , color contours) distribution. (For interpretation of the references to color in this figure legend, the reader is referred to the web version of this article.)

During upwelling relaxation, the alongshore jet and the corresponding cross-shelf current weaken (Fig. 8B, D and F). The greater weakening occurs over the inner shelves along the western and central sections where currents flow in the direction opposite to the one during upwelling. Along the eastern section, the eastward upwelling jet weakens and spatially shrinks, but the jet remains (also see Fig. 6). The landward currents in the bottom layers are substantially weakened over the shelf, yet, the cross-bay circulation in the Mirs Bay along the eastern section enhances as wind-induced vertical mixing weakens. Over the inner shelf, waters in the upper layer become more stratified and waters in the deeper layer thicken during upwelling relaxation. The vertical viscosity decreases dramatically in magnitude, particularly along the western and eastern shelves (Fig. 9B, D and F).

#### 4.2. Tidally modified upwelling circulation over the shelf

The tidal wave from the open ocean propagates southwestward along the NSCS shelf and intrudes into the PRE with the flooding-ebbing currents directing almost in a northwest-southeast direction (Zu et al., 2008). Fig. 10A and B shows the upwelling jet and salinity in the case without tidal forcing along the sections over the western and eastern shelves, which can be used to compare with the condition with tidal forcing. During the flood tide, the northwestward tidal currents oppose the northeastward upwelling alongshore currents and weaken currents in the whole water column over the shelf (Fig. 10A and B vs. E and F). In contrast, the southeastward ebbing currents reinforce the upwelling jet (Fig. 10A and B vs. C and D). The changes in the alongshore velocity are relatively strong in the upper water column during the ebb, but in the lower water column during the flood with the strongest change located at  $\sim 30\text{--}40$  m depth.

Although the tidal current either strengthens or weakens the landward salinity water intrusion in the bottom boundary layer, it is not strong enough to greatly modulate the wind-driven upwelling circulation. This is probably because the effect of flooding/ebbing current on the upwelling offsets each other by the alternative weakening/strengthening the intensity of upwelling alongshore current and thus onshore Ekman flow in the bottom layer. However, tides have limited effect in the subtidally averaged currents due to the nature of tidal periodicity.

#### 4.3. Estuary-shelf exchange

The intensity of the water exchange between the estuary and shelf is shown by the normal velocity component and salinity contours of the section at the entrance of the PRE (Fig. 11). During upwelling, the intrusion occurs mainly at the western bank and along the two deep channels. Strong intrusive currents at the western bank occupy the entire water column and extend eastward in the bottom layer. The velocity structures along the middle and eastern deep channels exhibit typical flow pattern of surface outflow and bottom inflow over the stratified water column. During upwelling relaxation, the intensity of the intrusion is substantially weakened at the western bank. However, the intrusion strengthens slightly and extends upward along the two deep channels while stratification is enhanced in the upper layer. The intrusion mainly occurs below the surface at both the western bank and in the eastern channels during upwelling relaxation.

The sub-tidal net water transport between the PRE and adjacent shelf is calculated by the integration of the residual currents normal to the section across the entrance of the PRE (Fig. 12). To eliminate the variation contributed by the river discharge, the volume of the river discharge is deducted from the net transport. The variation of net exchange between the shelf and the estuary is negatively correlated with the change in the alongshore wind component, or with the

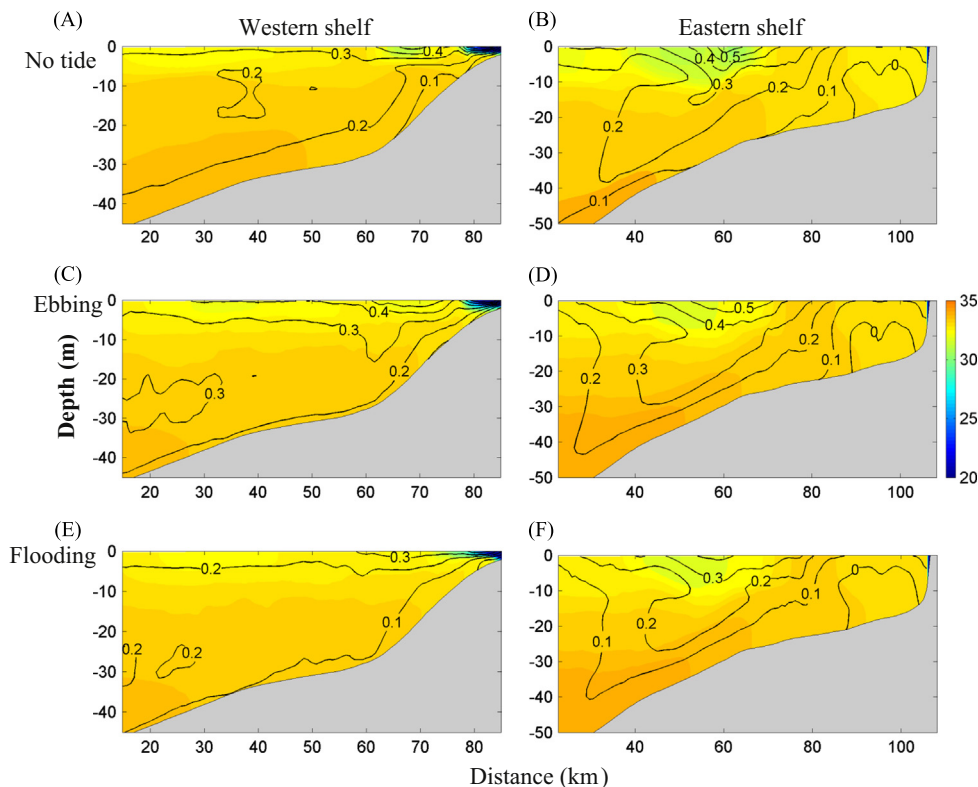


**Fig. 10.** Salinity (color contour) and along-shore current ( $u$ ,  $\text{m s}^{-1}$ , black contour) over western shelf (slice 130, left column) and over the eastern shelf (slice 285, right column) in the case forced by upwelling favorable wind and river discharge (A and B) and in the case forced by wind, river discharge and tides (C–F). All values are averaged during the upwelling period. The  $x$  axis is the distance (km) from the southern boundary to the northern boundary of the model domain, and the  $y$  axis is the water depths (m). (For interpretation of the references to color in this figure legend, the reader is referred to the web version of this article.)

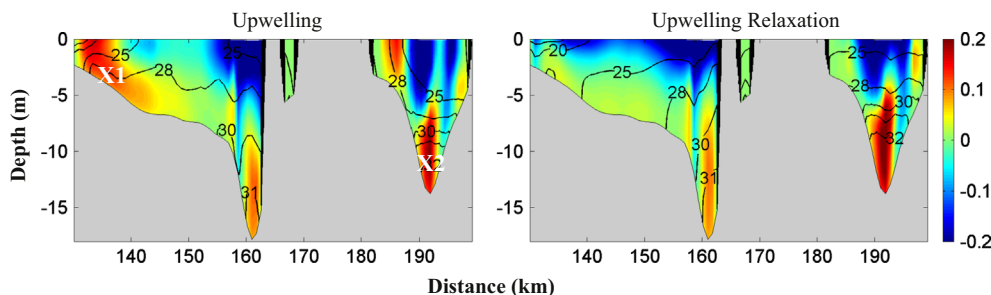


**Fig. 11.** Distribution of salinity (black contour) and velocity component ( $\text{m s}^{-1}$ , color contour) normal to the section across the entrance of PRE (Fig. 1). They are averaged during the upwelling (left panel) and upwelling relaxation (right panel), respectively. The axis is the distance (km) from the western boundary to the eastern boundary along the entrance, and the axis is the water depths (m). X1 and X2 represent the locations with relatively strong intrusive currents along the entrance of the PRE. (For interpretation of the references to color in this figure legend, the reader is referred to the web version of this article.)

intensity of upwelling circulation. Although the landward intrusive current below the surface is generally stronger during upwelling (Fig. 11), the net landward transport integrated along the entrance strengthens during upwelling relaxation and weakens during upwelling. This interesting phenomenon suggests that the relatively strong surface Ekman transport compensates the intrusive bottom current during upwelling, while the pre-existing upwelling circulation and the ceased seaward Ekman transport during upwelling relaxation enhance the net intrusive transport. Thus, it is not hard to conclude that during upwelling the water exchange rate between the shelf and estuary increases and the flushing time in the estuary reduces.

## 5. Dynamic analysis

The forcing mechanisms involved in the estuary–shelf circulation are analyzed by the corresponding depth-averaged along-shore

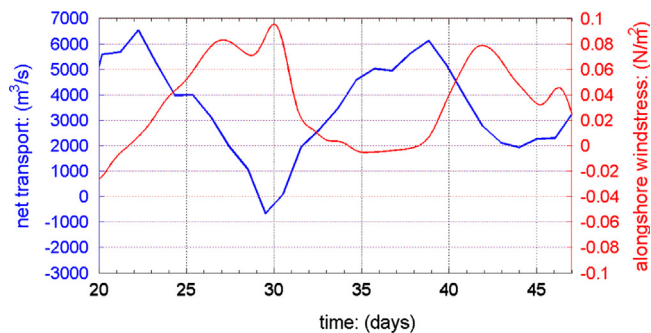


**Fig. 12.** Time series of the integrated net transport (blue line: with river discharge deducted) normal to the section across the entrance of the PRE and the wind stress (red line: 36-h smoothed) in the alongshore direction. The  $x$ -axis is the number of days from 1st, July, 2000. (For interpretation of the references to color in this figure legend, the reader is referred to the web version of this article.)

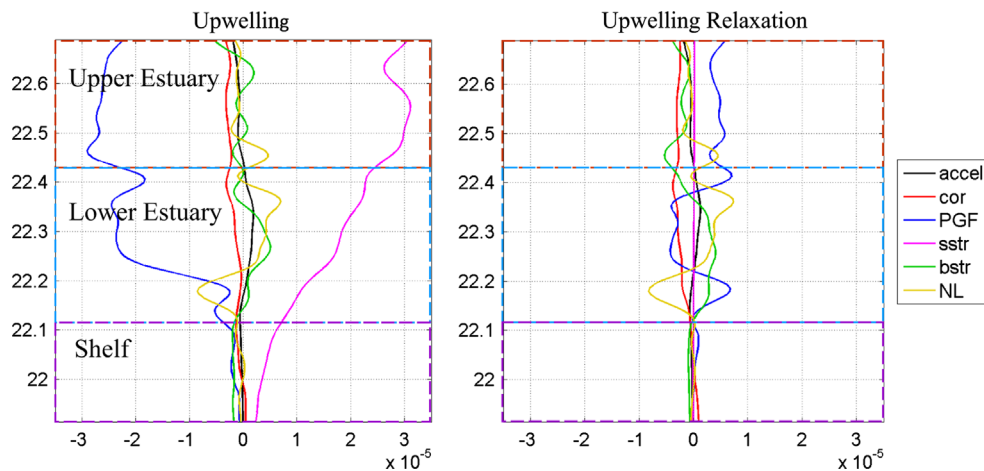


**Fig. 13.** Distribution of the terms ( $\text{m s}^{-2}$ ) in  $x$  component of the depth-averaged momentum balance from the shelf to the upper PRE in the box shown in Fig. 1B during (A) upwelling and (B) upwelling relaxation. The  $x$  axis is the magnitude of the terms, and the  $y$  axis is the latitude along the box in Fig. 1B. The red, blue, and purple boxes refer to the regions of upper estuary, lower estuary, and the shelf region, respectively. (For interpretation of the references to color in this figure legend, the reader is referred to the web version of this article.)

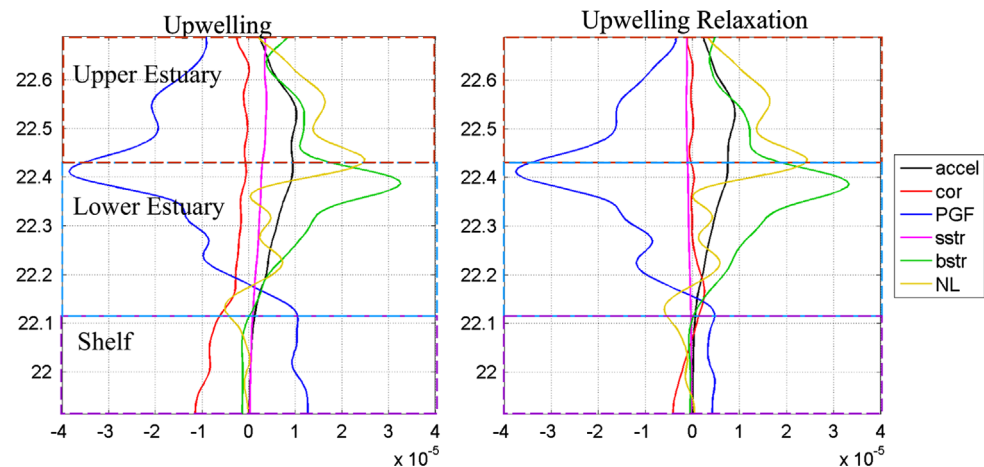


**Fig. 14.** Similar as Fig. 13, but for the terms ( $\text{m s}^{-2}$ ) in  $y$  component of the depth-averaged momentum balance.

( $x$ -direction in the model) and cross-shore ( $y$ -direction in the model) momentum Eqs. (1) and (2)

$$\frac{\partial U}{\partial t} = \underbrace{fV}_1 - \underbrace{\frac{1}{\rho_0} \frac{\partial P}{\partial x}}_2 + \underbrace{\frac{1}{\rho_0 D} \tau_s^x}_3 - \underbrace{\frac{1}{\rho_0 D} \tau_b^x}_4 - \underbrace{NL}_5 \quad (1)$$

$$\frac{\partial V}{\partial t} = -fU - \frac{1}{\rho_0} \frac{\partial P}{\partial y} + \frac{1}{\rho_0 D} \tau_s^y - \frac{1}{\rho_0 D} \tau_b^y - NL, \quad (2)$$

where ( $U, V$ ) are depth-averaged barotropic velocity in ( $x, y$ );  $f$  is the Coriolis parameter;  $\rho_0$  is the reference density;  $P$  is depth-averaged pressure;  $D$  is the total water depth; ( $\tau_s^x, \tau_s^y$ ) are the surface wind stress components; ( $\tau_b^x, \tau_b^y$ ) are the bottom stress components; and  $NL$  represents the nonlinear horizontal advection and horizontal viscosity terms. The terms in the above equations are defined as: acceleration (term 1, *accel*); Coriolis force (term 2, *cor*); pressure gradient force (term 3, *PGF*); surface wind stress (term 4, *sstr*); and bottom stress (term 5, *bstr*). The sum of terms 4 and 5 is referred to as the shear stress (*sbstr*) term and the sum of terms 2 and 3 as the ageostrophic term (*ageo*). The characteristics of the fundamental dynamics around the PRE are presented by the directional term balance of Eqs. (1) and (2) in Figs. 13 and 14. The mechanisms for the intrusive currents at the western bank and in the eastern

channel are illustrated by the time series of their respective momentum balance in Figs. 15 and 16.

### 5.1. Directional forcing

In the PRE, the major balance in the  $x$ -direction (Fig. 13) is between *PGF* and *sstr* as a result of the water piling up due to the eastward wind over the eastern shoulder of the estuary during upwelling. The wind effect and thus *PGF* weakens in the water column towards the entrance as water depth increases. Wind stress tends to balance the rest of the terms in Eq. (1) over the shelf in  $x$  direction. As the wind relaxes, *PGF* in  $x$  direction changes sign in the upper estuary to balance the negative *cor* and *bstr* as the buoyant river water flows southward. *PGF* decreases substantially in the lower estuary and mainly balances the locally amplified nonlinearity. Over the shelf off the PRE, all terms along the  $x$ -direction are very small during the relaxation.

With the much smaller wind forcing in the  $y$ -direction, the momentum balance (Fig. 14) is distinguished by the formation of negative *PGF* inside the PRE due to freshwater input, which balances both *NL* and *bstr*. It demonstrates a dominant advective gravitational circulation in the two-layer estuary (also see Figs. 6 and 8). Very strong *PGF* occurs in the central estuary where the front is located (Fig. 7). This balance is mainly controlled by

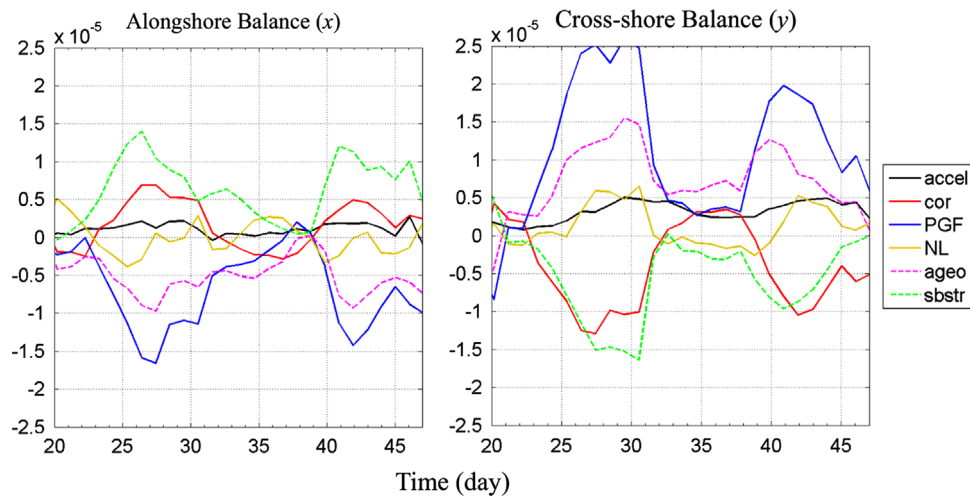


**Fig. 15.** Time series of terms ( $\text{m s}^{-2}$ ) in alongshore ( $x$ , left panel) and cross-shore ( $y$ , right panel) depth-averaged momentum balances at point X1 (shown in Fig. 11) over the western bank at the entrance. The “ageo” term is the sum of “PGF” and “cor” terms, and the “sbstr” term is the sum of the “sstr” and “bstr” terms or shear stress. The x-axis is the number of days from 1st, July, 2000.

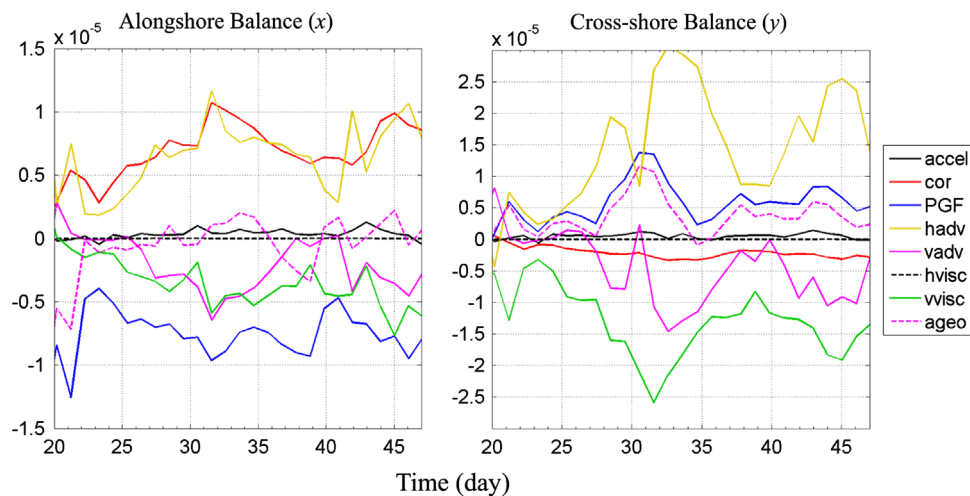


**Fig. 16.** Time series of terms in alongshore ( $x$ , left panel) and cross-shore ( $y$ , right panel) depth-dependent momentum balances ( $\text{m s}^{-2}$ ) at X2 (shown in Fig. 11) in the eastern channel at water depth of  $\sim 12$  m. The “ageo” term is the sum of “PGF” and “cor” terms. The x-axis is the number of days from 1st, July, 2000.

both the river discharge and tidal residual current, and it varies little in the estuary during upwelling and upwelling relaxation. Over the shelf, the balance turns into a geostrophic balance, in which a northward *PGF* forms an eastward alongshore geostrophic current during upwelling. This geostrophic balance relaxes as the upwelling wind relaxes. In all cases, the rotational effect is relatively small in the upper estuary and northern part of the lower estuary but it becomes important in the southern part of the lower estuary when southward *PGF* turns northward.

## 5.2. Forcing of intrusion

Fig. 11 clearly shows that there are two types of intrusive current from the shelf into the estuary: they are the western intrusion in the entire water column and the bottom intrusion in the deep channels to the east. To identify their forcing processes, we use the time series of the depth-averaged momentum term balances from Eqs. (1) and (2) at X1 (location shown in Fig. 11) in the western intrusion (Fig. 15), and a depth-dependent momentum Eqs. (3) and (4) at X2 ( $\sim 12$  m depth, location shown in Fig. 11) in the eastern channel (Fig. 16). The depth-dependent momentum

equations are

$$\frac{\partial u}{\partial t} = \underbrace{fv}_2 - \underbrace{\frac{1}{\rho_0} \frac{\partial p}{\partial x}}_3 + \underbrace{vvis}_4 + \underbrace{hadv + vadv}_5 \quad (3)$$

$$\frac{\partial v}{\partial t} = -fu - \frac{1}{\rho_0} \frac{\partial p}{\partial y} + vvis + hadv + vadv, \quad (4)$$

where  $(u, v)$  are depth-dependent velocity;  $p$  is depth-dependent pressure;  $(vvis)$  are vertical viscosity; and  $(hadv, vadv)$  are horizontal and vertical momentum advection. Other terms are analogous to those in Eqs. (1) and (2). Horizontal viscosity is neglected here. Along the  $x$ -direction at X1 of the western bank, negative *PGF* and *bstr* amplify during the upwelling favorable wind (Fig. 15). A positive *cor*, or the landward geostrophic current, forms while the residual of *PGF* and *cor* or *ageo* is balanced by the positive shear stress, *sbstr*, in the water column. From a depth-averaged vorticity equation, Gan et al. (2013) found that the along-shore pressure gradient force over the variable shelf topography arises from the vorticity formation due to the difference of surface and bottom stress curls as a result of flow-topography interaction. Clearly, both geostrophic and net landward Ekman transports contribute to the net intrusive current in the water column while

the alongshore current accelerates eastward.  $PGF$  weakens substantially and is balanced by  $bstr$  when the upwelling wind relaxes. The westward shelf current ( $cor < 0$ ) forms the seaward bottom Ekman transport at this time.

The balance in the  $y$  direction at X1 shows a northward  $PGF$  that maintains the geostrophic alongshore current (Fig. 15). Meanwhile, the residual of  $PGF$  accelerates current northward, and balances  $sbstr$  (or,  $bstr$ , because the wind is very small in the  $y$ -direction) to form gravitational circulation in the stratified water.

Along the  $x$ -direction at X2 in the eastern channel, positive  $cor$ , or the northward intrusive current, prevails during both upwelling and upwelling relaxation periods. It is quite interesting to note that the intrusion in this deep channel, with horizontal scale of  $\sim 5$  km, is largely caused by the meridional geostrophic current (Fig. 16). The balance in alongshore direction ( $x$ ) shows that the intrusion of the geostrophic current is strengthened during upwelling relaxation, in which the cross-channel  $PGF$  is formed as a result of the cross-channel gradient of dynamic height induced by the river plume, as shown by the salinity distribution in Fig. 11. The  $hadv$  in  $x$  direction is chiefly balanced by the corresponding  $vadv$ , reflecting the shoreward and upward momentum transport while shelf water intrudes into the estuary. In the cross-shelf ( $y$ ) direction, the positive  $PGF$  balance  $vvis$  to form the landward gravitational current, while horizontal momentum advection compensates the vertical advection similar to that in the  $x$ -direction. Clearly, in addition to the gravitational effect of the two-layer flow, the northward current can also be driven by positive  $PGF$  that is set up by the upwelling wind forcing over the adjacent shelf.

## 6. Summary

We have developed a high resolution coupled estuary–shelf model with realistic topography and forcing for the PRE and adjacent shelf to investigate the three-dimensional, time-dependent circulation in the estuary and adjacent shelf. We analyze the responses of the sub-tidal coupled shelf–estuary circulation to the multi-forcing of buoyancy from river discharge, tide, and upwelling/upwelling relaxation monsoon wind in the PRE and adjacent shelf during summer. The comprehensive investigation in this study provides many findings that are critical and previously unknown to the circulation dynamics in the region.

In the PRE, the circulation varies in the axial direction due to the corresponding variable effects of wind, tide, river discharge, topography, and the influence from the shelf. Seaward gravitational outflow is the dominant feature of the upper estuary and northern part of the lower PRE, where the surface flow pattern also varies with the upwelling winds. The circulation in the southern part of the lower PRE is governed by both gravitational circulation and geostrophic intrusive current from the shelf.

Over the shelf off the PRE, upwelling circulation strengthens with the increase of shelf slope and/or stratification, but weakens with enhanced vertical mixing due to local topography or tides. The interaction between the circulation and the plume largely shapes the stratification over the shelf and controls the cross-shelf (estuary) circulation. The ebbing/flooding tides strengthen/weaken the alongshore current and seaward/landward cross-shelf circulation during upwelling. Relatively strong tidal modulation of the upwelling circulation occurs in the surface layer during the ebb tide, but in the bottom layer during the flood tide. Although the flood/ebb currents enhance the cross-shelf exchange, their phases are opposite to the wind-driven shelf current, and the overall tidal effect on the wind-driven upwelling circulation is not significant.

The water exchange between the estuary and adjacent shelf exists during both upwelling and upwelling relaxation winds. The intrusion occurs mainly at the western bank and along the two deep channels during upwelling and upwelling relaxation. The exchange rate between the shelf and the PRE strengthens during upwelling, but weakens during upwelling relaxation when the surface Ekman transport decreases greatly. The tidal effect has only limited contribution to the exchange rate over sub-tidal time scale.

The landward intrusions over the western bank and in the deep channels show the importance of a geostrophic intrusive current due to westward  $PGF$  and a gravitational intrusive current due to the northward  $PGF$ , which are controlled by the alongshore variation of the wind-driven upwelling circulation and by the buoyancy forcing of the river plume, respectively.

## Acknowledgments

This research was supported by the National Natural Science Foundation of China (NSFC) under Project 41006012, by Hong Kong's Research Grant Council under Projects GRF612412 and N\_HKUST627/13 and by Centre for Marine Environmental Research and Innovative Technology (MERIT) under Projects AOE/P-04/04-5-II and VPRDO09/10.SC04. We are grateful to Huang Wei for processing the satellite remote sensing data, to Hong Kong Maritime Department for providing the bathymetry in Hong Kong waters and to Hong Kong Observatory for providing wind data.

## References

- Boyer, T.P., Levitus, S., Antonov, J.I., Locarnini, R.A., Garcia, H.E., 2005. Linear trends in salinity for the world ocean, 1955–1998. *Geophys. Res. Lett.* 32, L01604.
- Chapman, D.C., 1985. Numerical treatment of cross-shelf open boundaries in a barotropic coastal ocean model. *J. Phys. Oceanogr.* 15, 1060–1075.
- Dong, L.X., Su, J.L., Wong, L.A., Cao, Z.Y., Chen, J.C., 2004. Seasonal variation and dynamics in the Pearl River plume. *Cont. Shelf Res.* 24, 1761–1777.
- Fletcher, R.A., 1976. A tidal model of the north-west European continental shelf. *Mem. Soc. R. Sci. Liège* 6 (10), 141–164.
- Gan, J., Allen, J.S., 2005. On open boundary conditions for a limited area coastal model off Oregon. Part 1: Response to idealized wind forcing. *Ocean Model.* 8, 115–133.
- Gan, J., Cheung, A., Guo, X., Li, L., 2009a. Intensified upwelling over a widened shelf in the northeastern South China Sea. *J. Geophys. Res.* 114, C09019.
- Gan, J., Li, L., Wang, D., Guo, X., 2009b. Interaction of a river plume with coastal upwelling in the northeastern South China Sea. *Cont. Shelf Res.* 29, 728–740.
- Gan, J., Ho, H.S., Liang, L., 2013. Dynamics of intensified downwelling circulation over a widened shelf. *J. Phys. Oceanogr.* 43, 80–94.
- Haidvogel, D.B., Arango, H.G., Hedstrom, K., Beckmann, A., Malanotte-Rizzoli, P., Shchepetkin, A.F., 2000. Model evaluation experiments in the North Atlantic Basin: Simulations in nonlinear terrain-following coordinates. *Dyn. Atmos. Oceans* 32, 239–281.
- Ji, X., Sheng, J., Tang, L., Liu, D., Yang, X., 2011a. Process study of circulation in the Pearl River Estuary and adjacent coastal waters in the wet season using a triply-nested circulation model. *Ocean Model.* 38, 138–160.
- Ji, X., Sheng, J., Tang, L., Liu, D., Yang, X., 2011b. Process study of dry-season circulation in the Pearl River Estuary and adjacent coastal waters using a triply-nested coastal circulation model. *Atmos.–Ocean* 49 (2), 138–162.
- Large, W.G., Pond, S., 1981. Open ocean momentum flux measurements in moderate to strong winds. *J. Phys. Oceanogr.* 11, 324–336.
- Lu, Z.M., Gan, J., this issue. Controls of seasonal variability of phytoplankton blooms in the Pearl River Estuary. *Deep Sea Res.* II. [doi: 10.1016/j.dsr2.2013.12.010].
- Mao, Q., Shi, P., Yin, K., Gan, J., Qi, Y., 2004. Tides and tidal currents in the Pearl River Estuary. *Cont. Shelf Res.* 24, 1797–1808.
- Mellor, G.L., Yamada, T., 1982. Development of a turbulence closure model for geophysical fluid problems. *Rev. Geophys. Space Phys.* 20, 851–875.
- Orlanski, I., 1976. A simple boundary condition for unbounded hyperbolic flows. *J. Comp. Phys.* 21, 251–269.
- Ou, S., Zhang, H., Wang, D., 2007. Horizontal characteristics of buoyant plume off the Pearl River Estuary during summer. *J. Coast. Res. Spec. Issue* 50, 652–657.
- Shchepetkin, A.F., McWilliams, J.C., 2005. The Regional Ocean Modeling System: a split-explicit, free-surface, topography following coordinates ocean model. *Ocean Model.* 9, 347–404.
- Sheng, J., Tang, L., Ji, X., 2010. An examination of seasonal mean circulation and salinity distributions in the Pearl River Estuary of China using a triply-nested

- coastal ocean circulation model. In: Proceedings of 11th Estuarine and Coastal Modeling, pp. 108–127.
- Song, Y., Haidvogel, D.B., 1994. A semi-implicit ocean circulation model using a generalized topography-following coordinate system. *J. Comp. Phys.* 115 (1), 228–244.
- Su, J., 2004. Overview of the South China Sea circulation and its influence on the coastal physical oceanography outside the Pearl River Estuary. *Cont. Shelf Res.* 24, 1745–1760.
- Wong, L.A., Chen, J.C., Xue, H., Dong, L.X., Su, J.L., Heinke, G., 2003a. A model study of the circulation for the Pearl River Estuary (PRE) and its adjacent coastal waters 1, Simulations and comparison with observations. *J. Geophys. Res. Oceans* 108 (C5), 3156.
- Wong, L.A., Chen, J.C., Xue, H., Dong, L.X., Guan, W.B., Su, J.L., 2003b. A model study of the circulation in the Pearl River Estuary (PRE) and its adjacent coastal waters: 2. Sensitivity experiments. *J. Geophys. Res. Oceans* 108 (C5), 3157.
- Xue, H., Chai, F., Wong, L.A., Chen, J.C., 2001. Zhujiang (Pearl River) estuarine circulation model. In: Xue, H., Chai, F., Xu, J. (Eds.), *Oceanography in China*, 13. China Ocean Press, p. 254.
- Zu, T., Gan, J., 2009. Process-oriented study of the circulation and river plume in the Pearl River Estuary: Response to the wind and tidal forcing. *Adv. Geosci., Ocean Sci. Ser.* b672-v12-ch16.
- Zu, T., Gan, J., Erofeeva, S.Y., 2008. Numerical study of the tide and tidal dynamics in the South China Sea. *Deep-Sea Res.* 1 55, 137–154.